Iterative reconstruction for few-view grating-based phase-contrast CT —An in vitro mouse model

2013 EPL 102 48001

(http://iopscience.iop.org/0295-5075/102/4/48001)

A Letters Journal Exploring the Frontiers of Physics

May 2013

EPL, **102** (2013) 48001
doi: 10.1209/0295-5075/102/48001

www.epljournal.org

Iterative reconstruction for few-view grating-based phase-contrast CT —An in vitro mouse model

T. Gaass[1], G. Potdevin[2], M. Bech[2], P. B. Noël[3], M. Willner[2], A. Tapfer[2], F. Pfeiffer[1,2] and A. Haase[1]

[1] *Zentralinstitut für Medizintechnik, Technische Universität München - Boltzmannstr 11, 85748 Garching, Germany, EU*
[2] *Department of Physics, Technische Universität München - James-Franck-Str. 1, 85748 Garching, Germany, EU*
[3] *Department of Radiology, Technische Universität München - Ismaninger Str. 22, 81675 Munich, Germany, EU*

received 15 January 2013; accepted in final form 13 May 2013
published online 6 June 2013

PACS 87.57.nf – Reconstruction
PACS 87.57.Q- – Computed tomography
PACS 87.64.mh – Phase contrast and DIC

Abstract – The aim of this work is to investigate the improvement of image quality in few-view grating-based phase-contrast computed tomography (PCCT) applications via compressed sensing (CS) inspired iterative reconstruction on an *in vitro* mouse model. PCCT measurements are performed on a grating-based PCCT setup using a high-brilliance synchrotron source and a conventional tube source. The sampling density of the data is reduced by a factor of up to 20 and iteratively reconstructed. It is demonstrated that grating-based PCCT intrinsically meets the major conditions for a successful application of CS. Contrast fidelity and the reproduction of details is presented in all reconstructed objects. The feasibility of the iterative reconstruction on data generated with a conventional X-ray source is illustrated on a fluid phantom and a mouse specimen, undersampled by a factor of up to 20.

Introduction. – X-ray phase-contrast computed tomography (PCCT) techniques acquire information about the real part of the refractive index δ corresponding to an X-ray phase-shift. One particularly interesting implementation of PCCT is a setup based on a grating interferometer. This approach for the retrieval of differential phase information was already successfully implemented at X-ray synchrotron radiation sources [1–5]. Since grating-based PCCT acquisition can also be realized with conventional X-ray tubes [6–8], this method is in particular of interest for potential future medical examinations [9].

It has been demonstrated that grating-based PCCT projections can be reconstructed using filtered backprojection (FBP), by implementing an altered filter [10]. As in conventional absorption-based CT, one has to obey the Nyquist-Shannon theorem when sampling an object. Consequently, in order to generate a high-resolution image without artifacts a large number of projections is necessary. Ultimately, the goal is to translate PCCT into clinical applications, where a large number of projections would cause a undesirable large radiation exposure. While precise dose optimization has yet to be performed when using PCCT, the ALARA principle suggests maximal dose reduction prior to clinical applications. The straightforward way to save measurement time, as well as dose is to reduce the number of projection images per gantry rotation. However, conventional FBP reconstruction of such undersampled data sets results in images impaired by aliasing artifacts. Donoho *et al.* demonstrated that, by using compressed sensing (CS), under certain conditions it is possible to recover artifact-free images from a drastically smaller number of measurements [11–14]. Employing *a priori* information about the reconstructed PCCT image in a nonlinear iterative reconstruction framework poses a very effective way to accomplish an artifact-free reconstruction of few-view, thus dose-reduced PCCT acquisitions.

We investigate the performance of a compressed sensing inspired iterative reconstruction for PCCT data. As simulation studies have been reported extensively [15,16] and previous publications [15,17] could already demonstrate the performance of compressed sensing on PCCT data of simple objects obtained with highly brilliant synchrotron radiation, we present a comprehensive performance assessment of a CS-inspired iterative reconstruction for PCCT

within this study. In addition to simulations and phantom measurements, we demonstrate the feasibility of the CS-based algorithm on few-view measurements of *in vitro* mouse specimen using both, a high-brilliance synchrotron source and a conventional X-ray tube. Evaluating the applicability to tomograms acquired with a conventional X-ray source constitues the special focus of this work, aiming to assess the feasibility of PCCT in a dose-limited clinical setting.

The general principle underlying compressed sensing based reconstructions can be described as follows: If the original signal f is sparse and an incoherent sampling basis Φ is used to measure this signal, it is possible to recover the signal, even when violating the Nyquist limit by using sparsity as prior knowledge in a nonlinear reconstruction that enforces sparsity.

Hence, the successful application of compressive sampling calls for the prerequisites of (*transform*) *sparsity*, *incoherent sampling* and a *nonlinear reconstruction*, that enforces sparsity. In the following we provide details on the overlap of PCCT and said conditions, as well as an overview of the employed theoretical framework.

Sparsity. A single image is considered sparse if it is populated primarily with zero entries and is thus by nature easily compressible. In medical tomography in rare cases such as angiography, the object to be reconstructed is naturally sparse. However, in general one has to find a representation in a basis Ψ, which introduces sparsity to the data.

Since high sparsity is essential for the successful application of compressed sensing based reconstructions, it is crucial to find a transform domain suitable for the present data. For natural images and human perception, developments in lossless data compression [18] demonstrated that the Wavelet transform is a very efficient sparsifying operation.

Additionally, the finite-difference transformation was previously implemented as sparsity transformation in noise reduction algorithms [19]. Applying both transformations separately results in a very efficient sparcification of tomographic images, emphasizing different image features, such as small details and edges.

Maximizing sparsity, hence minimizing the so-called l_0-norm poses a very challenging computational task. Donoho [11] was able to prove that, when dealing with ill-posed systems of linear equations such as the present reconstruction task, the solution of minimal l_1-norm (eq. (1)) simultaniously is the sparsest solution with very high probability:

$$\|x\|_p := \left(\sum_{n=0}^{N-1} \|x\|^p \right)^{1/p} \quad \text{with} \quad p = 1, x \in C. \tag{1}$$

The l_1-minimization poses a problem of less complexity which, in contrast to the l_0-norm minimization, is solvable in moderate computational time. Thus the algorithm within this work employs l_1-norm minimization in order to find the sparsest solution.

Incoherence. It is well understood that undersampling, hence decreasing the sampling density below the limit of Nyquist, causes aliasing artifacts [20]. Considering data acquisition in a Cartesian Fourier domain (k-space), equidistant undersampling together with simple zero-filling missing data points leads to the superposition of shifted replicas of the original signal or image. This causes ambiguities precluding any possibility to recover the original signal. An acquisition scheme, incoherent to the chosen sparsity transform basis, on the contrary causes signal to transfer from the sparsely distributed nonzero values to formerly zero valued coefficients. This signal exchange manifests as noise-like artifacts in the reconstructed image, providing the possibility to still distinguish the original nonzero-valued coefficients of the sparse signal.

From the definition of *mutual coherence* μ [21]

$$\mu := \sqrt{N} \max_{i,j} |\langle \phi_i, \psi_j \rangle| \tag{2}$$

one can derive, that, when using Cartesian sampling, incoherence has to be introduced by applying some sort of random sampling scheme, whereas incoherence is inherent when using radial sampling, as in CT imaging [14].

Reconstruction. In case of radial sampling, as applied in PCCT, the Nyquist criterion is satisfied if the maximal azimuthal distance does not exceed the distance between radial sampling points. Thus for a given base resolution of n, the required number of projection images n_p is

$$n_p = \frac{\pi}{2} \cdot n. \tag{3}$$

The sinograms subject to reconstruction are hence constructed as a subset of the full sinogram, where missing projections are substituted with zero entries.

The transformation of sinograms into real space is conventionally realized using filtered backprojection. A different approach, called regridding, was initially adapted to medical imaging by O'Sullivan [22] and further developed by Fessler *et al.* under the acronym NUFFT (nonuniform fast Fourier transform) [23]. The NUFFT algorithm interpolates a radially acquired k-space data set onto a Cartesian grid in order to apply a fast Fourier transform. Utilizing NUFFT rather than filtered backprojections simplifies the implementation of different reconstruction filters as well as sampling schemes and provides the possibility of fast forward and backward transformation during the subsequent iteration process.

According to the Fourier slice theorem, after a one-dimensional Fourier transform radial lines in k-space represent the acquired CT projections. In order to compensate for the differential nature of the acquired phase signal, the Hilbert filter [10] was implemented into the NUFFT algorithm. This leads to an initial, so-called minimal energy reconstruction of the zero-filled PCCT sinogram. Subsequently, this image is subject to an optimization process, approaching the sparsest solution in the aforementioned transformation domains.

Equation (4) summarizes the penalized minimization based reconstruction.

$$\text{Image} = \text{argmin}_f \left[\| \text{FT}(f) - y \|_2^2 + \lambda_{WL} \| \text{WL}(f) \|_1 + \lambda_{TV} \text{TV}(R) \right]. \quad (4)$$

The first term of eq. (4) denotes the data fidelity of the reconstruction by comparing the raw k-space data y with the Fourier transform (FT) of the resulting reconstruction f. The minimization of data fidelity is constrained with both the l_1-norm in the wavelet domain (WL) weighted by the penalty parameter λ_{WL} and the l_1-norm in the finite-difference domain (or total variation (TV)) weighted by λ_{TV}.

The algorithm used for optimization is based on a procedure initially implemented in Matlab (Mathworks, Natick, US) for radial MRI by Lustig (`http://www.stanford.edu/~mlustig/SparseMRI.html`). The algorithm uses a nonlinear conjugate gradient approach in order to solve the minimization problem together with the Fletcher-Reeves method for search direction updates after each iteration step [24].

Experimental. – To comprehensively evaluate the applicability of the implemented algorithm, a numerical phantom, as well as undersampled measurements using a high-brilliance X-ray source and a conventional source were conducted. Using NUFFT and the iterative reconstruction, images were generated for qualitative and quantitative comparison. The windowing of the reconstructed images in the results section was chosen based on the region of interest (ROI) evaluation. The minimum and maximum in the image structure of interest was detected and set to 10% and 90% of the gray scaling, unless otherwise stated.

Numerical simulation. In order to initially assess the performance of the implemented algorithm on phase-contrast CT, data acquisition was simulated on a numerical Shepp-Logan phantom of matrix size 256^2. The phantom was sampled by inversely applying a differential PCCT version of the NUFFT algorithm using 25 projections, corresponding to an undersampling factor of 16. Subsequently the implemented reconstruction was applied to the data set using both the wavelet and total variation transformation. While fig. 1(a) depicts the original representation, fig. 1(b) displays the NUFFT reconstruction of the few-view data set. The 16-fold undersampled reconstruction shows strong streaking artifacts resulting in complete loss of detail information and sharpness in contrast edges. Figure 1(c) depicts the resulting iterative reconstruction. Streaking artifacts are successfully suppressed, without any perceptual loss in details. The profiles presented in fig. 1(d) demonstrate that the algorithm effectively reduced streaking artifacts while preserving edge sharpness and contrast properties of the reconstructed volume. When compared to the artifact impaired profile (line in fig. 1(b)), the profile after iterative reconstruction (line in fig. 1(c)) is free of any aliasing and almost not distinguishable from the profile crossing the original object (line in fig. 1(a)).

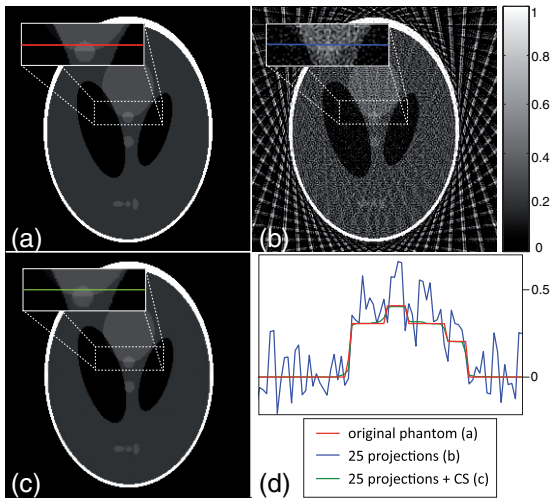

Fig. 1: (Colour on-line) (a) Nyquist-sampled reconstruction of the Shepp-Logan phantom with a matrix size of 256×256; (b) image reconstructed from 25 projection images using NUFFT; (c) reconstruction from 25 projection images using the iterative algorithm; (d) plot of one single line through a part of the reconstruction, marked within the magnified region.

The numerical Shepp-Logan phantom indicates the possibility to generate images, indistinguishable from the original reconstruction with an undersampling factor of 16. Presumably, even lower sampling densities are applicable without losing vital information when using this object. While the Shepp-Logan phantom is a satisfying object to simulate biological specimen, especially the human head, its strong contrast properties and elliptical shapes are unnaturally beneficial for both total variation and projection sampling when compared to actual brain data. Generally speaking CS-like reconstructions are increasingly effective with increasing sparsity, which applies for piecewise constant objects in the case of total variation transformation and images that are naturally sparse in the case of wavelet transformation [25,26]. Consequently, it is crucial to investigate more complex objects.

In vitro. To evaluate the performance of the implemented algorithm on experimental data, we reconstructed a data set comprising both soft tissue and bone structures. In order to observe the results of the proposed algorithm when dealing exclusively with aliasing artifacts, rather then noise and beam hardening, the presented data was acquired using a synchrotron source at the European Synchrotron Radiation Facility (ESRF, beamline ID19, Grenoble, France). A formalin fixated mouse specimen was examined using a two-grating Talbot interferometer (grating periods: $p1 = 4.79\,\mu$m, $p2 = 2.40\,\mu$m; intergrating distance: $d(G1, G2) = 408\,$mm). 901 projections over 360 degrees with four phase steps were acquired at an X-ray energy of 35 keV and an exposure time of 1 s per

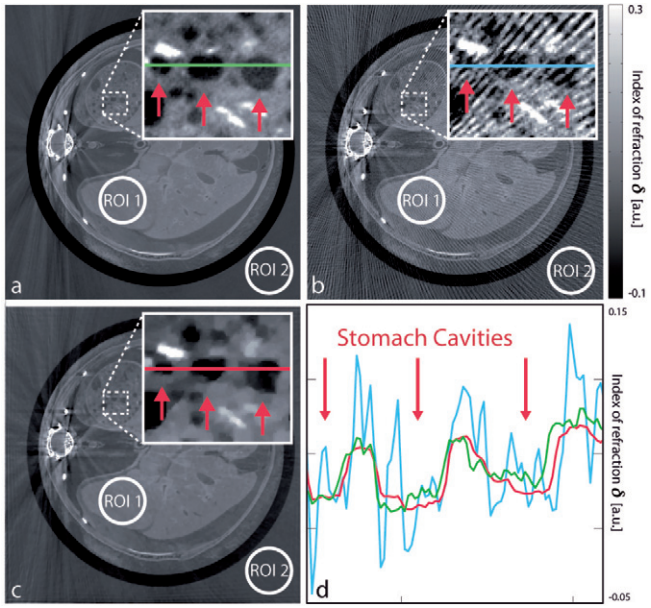

Fig. 2: (Colour on-line) (a) Reconstruction based on a PCCT sinogram with 901 projections, including the used regions of interest (ROI); (b) image reconstructed from 151 projections; (c) reconstruction from 151 projections using the iterative algorithm. The windowing was chosen for best visual appearance.

image. Using merely a number of 151 projections a 10-fold undersampled version of the original data was generated. The fully sampled reconstruction in fig. 2(a) exclusively shows phase wrapping artifacts from bone structures, while fig. 2(b) displays the zero-filling reconstruction impaired by additional aliasing artifacts. Figure 2(c) depicts the result of the iterative reconstruction with almost completly suppressed aliasing artifacts. As the theory of compressed sensing predicts, the algorithm is very effective when dealing with incoherent, or noise-like artifacts. Phase wrapping, as present in this data set, on the contrary are of different nature and consequently only weakly suppressed. Detail and contrast fidelity of the iterative reconstruction however are not impaired by the remaining artifacts as can also be observed in the line profiles presented in fig. 2(d).

In addition to the visual comparison, the synchrotron data set was quantitatively evaluated on the basis of a region of interest (ROI) analysis. The mean pixel value and standard deviation (STD) among the pixels comprised in the marked ROIs were calculated and are compared in table 1. The assessment shows that, while maintaining the original pixel intensities, the implemented algorithm was able to reduce the standard deviation within the ROIs by 35% compared to the undersampled reconstruction.

As mentioned above the proposed algorithm is based on the incoherence of alaising artifacts. Since this prerequisite is not met by the present bone streaks, these artifacts are recognised as vital image structure by the algorithm. However, the results demonstrate that the reconstruction algorithm can reduce undersampling artifacts very

Table 1: Mean pixel values and standard deviation within the regions of interest, depicted in fig. 2 for the fully sampled (FS), the undersampled (US) and the iterative reconstruction (IR) case.

	FS		US		IR	
	Mean δ	STD	Mean δ	STD	Mean δ	STD
ROI 1	0.061	0.006	0.082	0.025	0.061	0.007
ROI 2	-0.005	0.004	0.004	0.019	-0.003	0.003

effectively, even in the presence of additional phase wrapping artifacts due to bone structures.

In order to assess the algorithm on data acquired using a conventional X-ray source, two tomographic data sets were examined. Measurements conducted with a conventional X-ray source (an ENRAF rotating anode X-ray tube with a Molybdenum target) were performed using a three grating interferometer in a symmetrical Talbot-Lau geometry. All three gratings had a period of 5.4 μm and were separated by a distance of 87.5 cm. The two absorption gratings have approximately 50 μm high gold structures, while the 8 μm high nickel phase grating results in a π phase-shift for X-rays of 22.8 keV energy. The X-ray source was operated at a voltage of 35 kVp and had a total of 701 projections over 360 degree with 11 phase steps and 5 s exposure time each. PCCT images, especially those acquired with X-ray sources of low brilliance, are in addition to noise and streaking often impaired by cupping or dishing artifacts due to beam hardening [27]). Since TV is an enforcing piecewise constant representation, smooth intensity changes are translated into intensity steps, which leads to so-called stair-casing artifacts. As performed here a prior correction of these artifacts is necessary. The initial mouse specimen and fluid phantom reconstruction was post-processed to reduce the existing cupping artifact caused by beam hardening and subsequently resampled according to the aforementioned number of projections.

The reconstructin of an undersampled acquisition of a fluid phantom allowed exclusive focus on contrast fidelity of the iterative reconstruction when applied to PCCT data. The phantom comprised 6 polypropylene tubes, filled with saline solutions and pure liquids to generate a range of different phase-contrast signals (detailed description of the phantom in [28]). Data was acquired using a conventional X-ray source and an original sampling density of 701 projections. The reconstruction algorithm was applied to datasets with gradually decreasing number of projections up to an undersampling factor of 20.

Figure 3 presents a comparison of three different reconstruction approaches on the introduced fluid phantom data. Column 1 comprises reconstructions to a resolution corresponding to eq. (3). That is, by rebinning the raw data the base resolution of the sinograms subject to reconstruction is adapted to the number of projections and subsequently interpolated to the original matrix size. Evidently, this results in a significant reduction of details

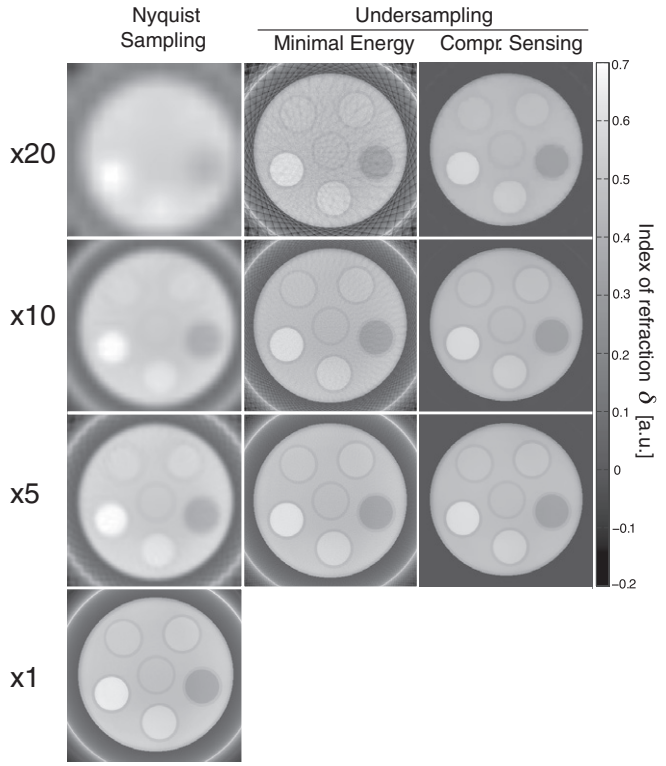

Fig. 3: Phase-contrast CT measurement of a fluid phantom with undersampling factors up to 20. Column 1: Nyquist sampling meeting the requirement $n_p = \frac{\pi}{2} n$ of the Nyquist-Shannon theorem; column 2: NUFFT minimal energy reconstruction, zero-filling not sampled data points; column 3: iterative reconstruction using both wavelet sparsity and TV minimization.

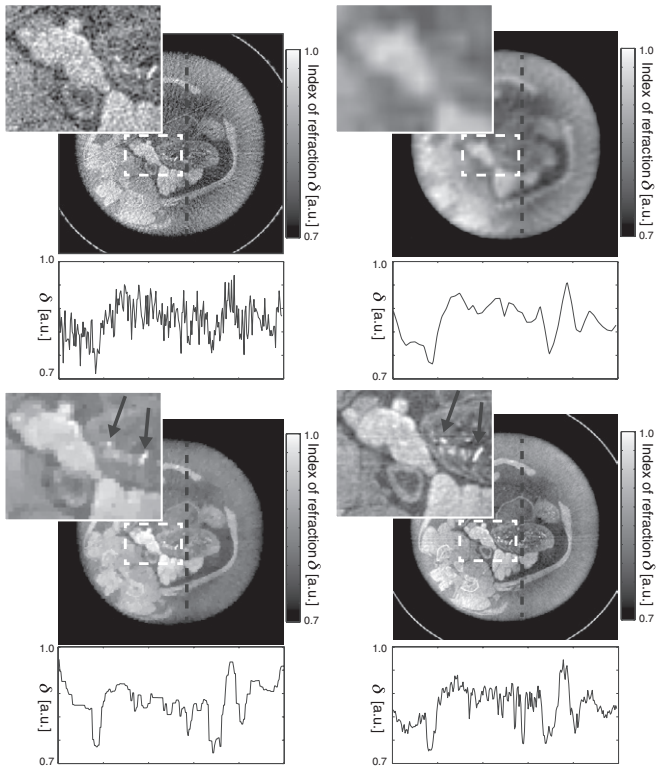

Fig. 4: Reconstructions of a transverse slice of a fixated, decalcified mouse. (a) NUFFT reconstruction of few-view undersampling ($n_p = 50$, $n = 318$); (b) few-view Nyquist sampling ($n_p = 50$, $n = 32$) interpolated to 318; (c) iterative reconstruction of few-view undersampling regaining image smoothness and resolving power comparable to the original; (d) fully sampled according to Nyquist ($n_p = 701$, $n = 318$).

to an extent of complete loss of information contained in the image. The reconstruction of undersampled data by zero filling (column 2) shows heavy streaking artifacts of increasing severity with decreasing number of used projections. Column 3 presents results of the iterative reconstruction in cases of three different undersampling factors (5, 10 and 20). When compared to the original fully sampled image almost no perceptual loss in image quality is observed in the iterative reconstruction. In fact, the quality of the proposed reconstruction algorithm outperforms even the fully sampled image up to an undersampling factor of 10, due to the suppression of noise.

The sensitivity of artifact reduction on solely soft tissue PCCT was evaluated on a tomographic data set of a formalin embedded, decalcified mouse specimen. The chosen slice comprises different signal intensities and fine details. Initially the object was sampled using 701 projections and reconstructed to a matrix size of 318^2. The performance of the algorithm was tested on a subset of only 50 of the original projections, hence an undersampling factor of 10.

The undersampled data set was reconstructed using zero filling (fig. 4(a)) and via rebinning (fig. 4(b)). Figure 4(c) displays the result of the application of the proposed algorithm, while fig. 4(d) comprises the reconstruction of the fully sampled acquisition. The application of the iterative reconstruction lead to a considerable reduction of not only alisaing artifacts, but also noise and apparent ring artifacts caused by the interpolation during NUFFT reconstruction. Additionally, residual cupping in the original data was corrected for in the iterative reconstruction, explaining the apperent change in contrast properties in the image center. Line profiles along the dashed black line clearly show that detailed information in fig. 4(a), as well as fig. 4(b) is almost completely lost due to aliasing and loss of resolution, respectively. The pixel profile crossing the iterative reconstruction not only displays a recovery of contrast and details, but also a suppression of noise, when compared to the profile of the fully sampled reconstruction. The squared regions of interest specially present details in the object (marked with arrows) which have successfully been recovered during the iterative reconstruction.

While the proposed algorithm was capable of efficiently suppressing streaking artifacts in all presented data sets, the artifact reduction comes at a price. The reconstruction of the two presented phantoms clearly benefit from

a strongly TV-weighted minimization. However, applying total variation regularization to data sets with fine structures or intensity gradients can possibly result in reduced spatial resolution. Consequently, the magnitude of TV weighting has to be well balanced in order to avoid overcompensation of artifacts.

Wavelet convolution has shown to be very effective in sparsifying natural images. Future application of compressive sampling algorithms for PCCT, however, call for further investigation of alternative bases. While the imaging basis of CT is fixed, in contrast to applications such as magnetic resonance imaging, the transform basis is interchangeable. As aforementioned the success of reconstructing few-view measurements strongly depends on the incoherence of the two bases. Consequently, the quality of the reconstruction can further benefit from an investigation of alternative transformations adapted to the particular application of PCCT.

Conclusion. – In summary we have demonstrated, both numerically and with experimental data, that the proposed iterative reconstruction effectively suppresses undersampling artifacts in phase-contrast CT. Therefore it is possible to reduce the number of projection images far below what the Nyquist-Shannon theorem conventionally postulates, while maintaining resolution, contrast and visibility of details. Even if no undersampling is performed the introduced algorithm offers the possibility to suppress noise, resulting in an image with improved SNR, when compared to the fully sampled reconstruction.

Current and future work comprises a detailed quantitative evaluation of the achievable resolution with the proposed reconstruction algorithm. Additionally the assessment of optimized penalty parameters poses a very important task. While many issues, such as image quality with respect to clinical significance or the speed of the algorithm are yet to be addressed, compressed sensing inspired reconstruction for phase-contrast CT may open the door for future advanced applications such as 4D-PCCT.

* * *

We acknowledge Irene Zanette and Timm Weitkamp for help during the sunchrotron experiments. We acknowledge financial support through the DFG Cluster of Excellence Munich - Center for Advanced Photonics (MAP), the DFG Gottfried Wilhelm Leibniz program and the European Research Council (ERC, FP7, StG 240142). This work was carried out with the support of the Karlsruher Nano Micro Facility (KNMF, `www.knmf.kit.edu`), a Helmholtz Research Infrastructure at Karlsruhe Institute of Technology (KIT).

REFERENCES

[1] Momose A., *Opt. Express*, **11** (2003) 2303.
[2] Weitkamp T., Diaz A., David C., Pfeiffer F., Stampanoni M., Cloetens P. and Ziegler E., *Opt. Express*, **13** (2005) 6296.
[3] Momose A., Yashiro W., Takeda Y., Suzuki Y. and Hattori T., *Jpn. J. Appl. Phys.*, **45** (2006) 5254.
[4] Pfeiffer F., Bunk O., David C., Bech M., Le Duc G., Bravin A. and Cloetens P., *Phys. Med. Biol.*, **52** (2007) 6923.
[5] Weitkamp T., David C., Bunk O., Bruder J., Cloetens P. and Pfeiffer F., *Eur. J. Radiol.*, **68** (2008) S123.
[6] Pfeiffer F., Weitkamp T., Bunk O. and David C., *Nature*, **2** (2006) 258.
[7] Bech M., Jensen T. H., Feidenhansl R., Bunk O., David C. and Pfeiffer F., *Phys. Med. Biol.*, **54** (2009) 2747.
[8] Donath T., Pfeiffer F., Bunk O., Grünzweig C., Hempel E., Popescu S., Vock P. and David C., *Invest. Radiol.*, **45** (2010) 445.
[9] Tapfer A. *et al.*, *Proc. Natl. Acad. Sci. U.S.A.*, **109** (2012) 15529.
[10] Pfeiffer F., Bunk O., Kottler C. and David C., *Nucl. Instrum. Methods Phys. Res. A*, **580** (2007) 925.
[11] Donoho D. L., *Communications*, **LIX** (2006) 797.
[12] Candes E. J. and Wakin M. B., *IEEE Signal Process. Mag.*, **25** (2008) 21.
[13] Lustig M., Donoho D. and Pauly J. M., *Magn. Reson. Med.*, **58** (2007) 1182.
[14] Lustig M., Donoho D. and Pauly J. M., *IEEE Signal Process. Mag.*, **25** (2008) 72.
[15] Sidky E. Y., Anastasio M. A. and Pan X., *Opt. Express*, **18** (2010) 10404.
[16] Han J., Bian J., Ritman E. L., Sidky E. Y. and Pan X., *Phys. Med. Biol.*, **57** (2012) 5245.
[17] Wang Z., Huang Z., Zhang L., Chen Z., Kang K., Yin H., Wang Z. and Stampanoni M., *J. X-Ray Sci. Technol.*, **19** (2011) 403.
[18] Usevitch B. E., *IEEE Signal Process. Mag.*, **18** (2001) 22.
[19] Rudin I. L., Osher S. and Fatemi E., *Physica D*, **60** (1992) 259.
[20] Rodney R. A., Glover G. H., Talbert A. J., Eisner R. L. and DiBianca F. A., *J. Comput. Assist. Tomogr.*, **3** (1979) 511.
[21] Candès E. J., in *Proceedings of the International Congress of Mathematicians, Madrid 2006*, Vol. **III** (EMS) 2007, p. 1433.
[22] O'sullivan J. D., *IEEE Trans. Med. Imaging*, **4** (1985) 200.
[23] Fessler J., *J. Magn. Reson.*, **188** (2007) 191.
[24] Fletcher R. and Reeves C. M., *Comput. J.*, **7** (1964) 149.
[25] Bian J., Siewerdsen J. H., Han X., Sidky E. Y., Prince J. L., Pelizzari C. A. and Pan X., *Phys. Med. Biol.*, **55** (2010) 2010.
[26] Han J., Bian J., Eaker D. R., Kline T. L., Sidky E. Y., Ritman E. L. and Pan X., *IEEE Trans. Med. Imaging*, **30** (2011) 606.
[27] Chabior M., Donath T., David C., Bunk O., Schuster M., Schroer C. and Pfeiffer F., *Med. Phys.*, **38** (2011) 1189.
[28] Tapfer A., Bech M., Pauwels B., Liu X., Bruyndonckx P., Sasov A., Kenntner J., Mohr J., Walter M. Schulz J. and Pfeiffer F., *Med. Phys.*, **38** (2011) 5910.